Numerical Heat Transfer, Part A, 41: 131–148, 2002

1040-7782/02 $12.00 + .00

NUMERICAL SIMULATION OF MIXED ELECTROOSMOTIC/PRESSURE DRIVEN MICROFLOWS

Prashanta Dutta
School of Mechanical and Materials Engineering, Washington State University, Pullman, Washington, USA

Ali Beskok
Department of Mechanical Engineering, Texas A&M University, College Station, Texas, USA

Timothy C. Warburton
Department of Mathematics and Statistics, University of New Mexico, Albuquerque, New Mexico, USA

A spectral element algorithm is developed to analyze mixed electroosmotic/pressure driven flows in complex two-dimensional geometries. The new algorithm exhibits spectral accuracy in resolving thin electric double layers. Mixed electroosmotic/pressure driven flows are simulated in straight channels. Electrokinetic pumping and the means of producing large pressure gradients in microchannels are explored. Finally, electroosmotic flow in a T-junction geometry is analyzed under various external electric field strengths. Flowrate in the T-junction is shown to vary linearly with the electroosmotic body forces in the Stokes flow regime.

INTRODUCTION

Recent developments in microfabrication technologies enabled a variety of miniaturized fluidic systems consisting of micronozzels, valves, pumps, and various other injection systems, which can be utilized in medical, pharmaceutical, and defense applications. These microfluidic systems require seamless integration of sample collection, separation, biological and chemical detection units with fluid pumping, flow control elements, and the necessary electronics on a single microchip. Compliance and reliability of the individual components with the entire microfluidic system poses many challenges. Subsystems like microvalves and micropumps with moving components are complicated to design and fabricate, and

Received 21 December 2000; accepted 27 July 2001.

A.B. would like to acknowledge the support provided by Texas Higher Education Council, Advanced Research Projects Program grant 000512-0418-1999. T.C.W. thanks DARPA F49620-96-1-0426 and DOE DE-FG02-98ER25346 for their support.

Address correspondence to Ali Beskok, Department of Mechanical Engineering, Texas A&M University, College Station, TX 77843-3123, USA. E-mail: abeskok@mengr.tamu.edu

NOMENCLATURE

D	dielectric constant	α	ionic energy parameter, $\frac{ez\zeta}{k_bT}$
$\vec{E}$	electric field	β	nondimensional parameter relating to α, ω, and h
E_x	streamwise component of electric field	δ^*	electric double layer displacement thickness
e	electron charge	η	nondimensional cross flow distance, y/h
h	half channel height	λ	Debye length, $1/\omega$
k_b	Boltzmann constant	μ	dynamic viscosity
n_o	bulk flow ion density	ξ	nondimensional streamwise distance, x/h
P	pressure	ρ_e	electric charge density
P^*	pressure normalized by $\mu u_p/h$	ρ_f	fluid density
$\dot{Q}$	volumetric flowrate per channel width	σ	conductivity
Re	Reynolds number	τ_w^*	nondimensional wall shear stress
T	absolute temperature	ϕ	External electric field potential
t	time	ψ	electroosmotic potential
U	nondimensional streamwise velocity, u/u_p	ψ^*	non-dimensional electroosmotic potential, ψ/ζ
U_{in}	nondimensional inlet velocity	ψ_c	electroosmotic potential at the channel center
u	streamwise velocity component	ζ	zeta potential
u_{in}	streamwise velocity at the inlet	ω	Debye Hũckel parameter
u_p	Helmholtz–Smoluchowski velocity		
$\vec{V}$	velocity vector		
z	valence		

they are prone to mechanical failure due to fatigue and fabrication defects. Electrokinetic body forces can be used in microfluidic control and fluid handling devices with nonmoving components. In this article we examine the electroosmotic transport.

Electroosmosis is one of the four major electrokinetic effects. It was first demonstrated by F. F. Reuss in 1809. This was followed later by the work of Helmholtz (1879) on the electric double layer (EDL) theory, which related the electrical and flow parameters for electrokinetic transport. In the early 1900s von Smoluchowski made seminal contributions to our understanding of electrokinetically driven flows, especially for conditions where the EDL thickness is much smaller than the channel height. Burgreen and Nakache presented analysis of mixed electroosmotic/pressure driven channel flows for thin two-dimensional channels, where the channel height becomes comparable to the EDL thickness [1]. This work was followed by theoretical analysis of electrokinetic flows in thin cylindrical capillaries [2, 3].

Recent experimental measurements of electrokinetically driven microflows were obtained by molecular fluorescence tagging (MFT) and microparticle image velocimetry techniques (μ-PIV) [4, 5]. Molho et al. [4] measured the velocity vector field in mixed electrokinetic/pressure driven microchannels and have shown that Joule heating effects and the corresponding changes in the fluid viscosity are secondary, compared with the streamwise pressure gradients. In a separate study, Paul et al. [5] utilized ultraviolet laser pulses to capture the flow patterns in mixed electrokinetic/pressure driven microchannel flows using a caged-dye fluorescence technique. A combined experimental and theoretical analysis of electroosmotic flows is presented by Cummings et al. [6], where the μ-PIV technique is used to

obtain the velocity distribution for straight channels and for crossing of two microchannels. Cummings et al. [7] also introduced the "ideal electroosmosis" concept, which reduces the flow field outside the EDL to a potential flow under some *specific* outer field boundary conditions. In a recent work by Herr et al. [8], velocity and dispersion rate measurements are presented for electroosmotic flows through cylindrical capillaries with nonuniform surface charge distribution. The experiments performed by the caged-dye fluorescense technique showed strong dependence of fluid velocity and dispersion rate on the surface charge. Jacobson et al. [9], developed parallel and serial mixing mechanisms in microcapillary networks and have shown that parallel mixing devices increase reliability of the microfluidic systems. Through a series of experiments, Polson and Hayes demonstrated electroosmotic flow control [10].

The past decade has also witnessed various numerical modeling and simulation efforts. Yang and Li [11] used the Debye–Hũckel approximation to develop a numerical algorithm for elecrokinetically driven liquid flows. They also identified the streaming potential effects and offered an explanation for deviations from the Poiseuille flow results for microscale liquid flows [12], first reported in [13]. Numerical simulation of microfluidic injection using electroosmotic forces through the intersection of two channels is presented by Patankar and Hu [14] using the Debye–Hũckel linearization. A finite difference algorithm for electroosmotic and electrophoretic transport and species diffusion was developed by Ermakov et al. [15], for two-dimensional complex geometry flow conduits. Bianchi et al. [16], studied electroosmotically driven microflows in T-junctions using a finite element formulation based on the Gouy–Chapman approximation. Liquid flow and forced convection heat transfer in electroosmotically driven microchannels are also analyzed using a finite difference method [17].

Considering the difficulties associated with performing experiments in microscales, it is desirable to develop reliable numerical models, that accurately describe electrokinetically driven flows in complex microgeometries. These numerical models can provide a further understanding of *coupled effects of the pressure, viscous, and inertial and electrokinetic forces* on fluid motion, and hence can be utilized for an *optimized microfluidic system* design prior to the hardware fabrication and experimental verification. In this article, we demonstrate utilization of electrokinetic forces for fluid handling, which leads to the concept of building micropumps and valves with nonmoving components. Such devices are not prone to mechanical failure due to fatigue. Moreover, they are more advantageous for biomedical applications, since cell damage due to pumping will be minimized, compared with the microsystems with moving surfaces, valves, and pistons.

This article is organized as follows: In the following section, the EDL concept is introduced. In the next section, the governing equations for electroosmotically driven flows are presented with underlying assumptions and approximations. The numerical algorithm used in the analysis of the problem, grid resolution, and numerical accuracy issues are also addressed. In the subsequent section, numerical simulation results are presented and compared with the previously reported analytical formulas. Next, numerical results of mixed electroosmotic/pressure driven flows in T-junctions are presented and flow manipulation techniques are demonstrated. Finally, discussions are presented.

ELECTRIC DOUBLE LAYER

The EDL forms due to the interaction of an ionized solution with static charges on dielectric surfaces. The static charge on the surface influences distribution of ions in the buffer solution, which is determined by the Poisson–Boltzmann equation [18, 19]:

$$\nabla^2(\psi) = \frac{-4\pi\rho_e}{D} \tag{1}$$

where the electric charge density ρ_e is given by

$$\rho_e = -2n_o ez \sinh\left(\frac{ez\psi}{k_b T}\right) \tag{2}$$

The Poisson–Boltzmann equation can be normalized using the zeta potential ζ and a characteristic length scale h in the form

$$\nabla^2(\psi^*) = \frac{-4\pi h^2 \rho_e}{D\zeta} = \beta \sinh(\alpha\psi^*) \tag{3}$$

where parameter β relates the ionic energy parameter α and characteristic length (h) to the Debye–Hũckel parameter ω as shown below:

$$\beta = \frac{(\omega h)^2}{\alpha}$$

$$\omega = \frac{1}{\lambda} = \sqrt{\frac{8\pi n_o e^2 z^2}{D k_b T}} \tag{4}$$

The solution of Eq. (3) gives the normalized electroosmotic potential distribution ψ^*, which decays exponentially fast within the EDL. An estimate of the EDL thickness can be obtained by $\lambda = 1/\omega$, and it is referred to as the Debye length. The Debye length is a function of the ion density n_o. For aqueous solutions at 25°C, the ion densities of 1 mol/m^3 and 100 mol/m^3 correspond to the Debye lengths of $\lambda = 10$ nm, and $\lambda = 1$ nm, respectively [18].

For our analysis we consider a two-dimensional channel and we assume that the zeta potential ζ is known, and it remains constant along the channel. Under these conditions Eq. (3) is simplified:

$$\frac{d^2\psi^*}{d\eta^2} = \beta \sinh(\alpha\psi^*) \tag{5}$$

If we multiply both sides of this equation by $2\frac{d\psi^*}{d\eta}$ and integrate with respect to η, we obtain the following relation:

$$\frac{d\psi^*(\eta)}{d\eta} = \left(\frac{\omega h}{\alpha}\right)\left[2\cosh(\alpha\psi^*) - 2\cosh(\alpha\psi_c^*)\right]^{\frac{1}{2}} \tag{6}$$

where both the electric potential and its spatial gradient at point η are represented as a function of the electric potential at the channel center (i.e., $\psi_c^* = \psi_{\eta=0}^*$). For the

cases where $\psi^*_{\eta=0} \to 0$, Eq. (6) can be integrated one more time with respect to η, resulting in [20]:

$$\psi^*(\eta^*) = \frac{4}{\alpha}\tanh^{-1}\left[\tanh\left(\frac{\alpha}{4}\right)\exp\left(-\sqrt{\alpha\beta}\ \eta^*\right)\right] \tag{7}$$

where η^* is the normalized distance from the wall (i.e., $\eta^* = 1 - |\eta|$).

In Figure 1, we present the numerical solution of the electroosmotic potential distribution as a function of various α and β values. Figure 1*a* shows the potential distribution for $\alpha = 1$. For small values of β, the EDL is thick and it covers the entire channel. As the value of β is increased, the EDL is confined to the channel walls, resulting in sharp variations in the electric potential. The electric potential distribution for $\alpha = 10$ is shown in Figure 1*b*. For a fixed value of β, comparisons of $\alpha = 1$ and $\alpha = 10$ curves show even faster decay of the electroosmotic potential for increased values of α.

GOVERNING EQUATIONS

The electroosmotic flow is created by applying an electrostatic field $\vec{E}$ in the streamwise direction, which can be represented as the gradient of an electric potential as $\vec{E} = -\nabla\phi$. The externally applied electric field interacts with the electric charge distribution in the EDL, and creates electrokinetic body forces on the fluid. The ionized incompressible flows with electroosmotic body forces are governed by the Navier–Stokes equations:

$$\rho_f\left(\frac{\partial\vec{V}}{\partial t} + (\vec{V}\cdot\nabla)\vec{V}\right) = -\nabla P + \mu\nabla^2\vec{V} + \rho_e\vec{E} \tag{8}$$

The incompressibility condition requires a divergence-free velocity field given by

$$\nabla\cdot\vec{V} = 0 \tag{9}$$

and subject to no-slip boundary conditions on the walls. Here ρ_e is determined from Eq. (3). The externally imposed electric potential (ϕ) is governed by

$$\nabla\cdot(\sigma\nabla\phi) = 0 \tag{10}$$

and the electric potential is subject to the insulating boundary conditions ($\nabla\phi\cdot\vec{n} = 0$) on the dielectric surfaces.

The main simplifying assumptions and approximations are as follows:

1. The fluid viscosity is *independent of the shear rate*. Hence, Newtonian fluid is assumed.
2. The fluid viscosity is *independent of the local electric field strength*. This condition is an *approximation*. Since the ion concentration and the electric field strength within the EDL is increased, the viscosity of the fluid may be affected. However, such effects are neglected in the current analysis, which considers only the dilute solutions.
3. The Poisson–Boltzmann Eq. (3) is valid. Hence the ion convection effects are negligible.

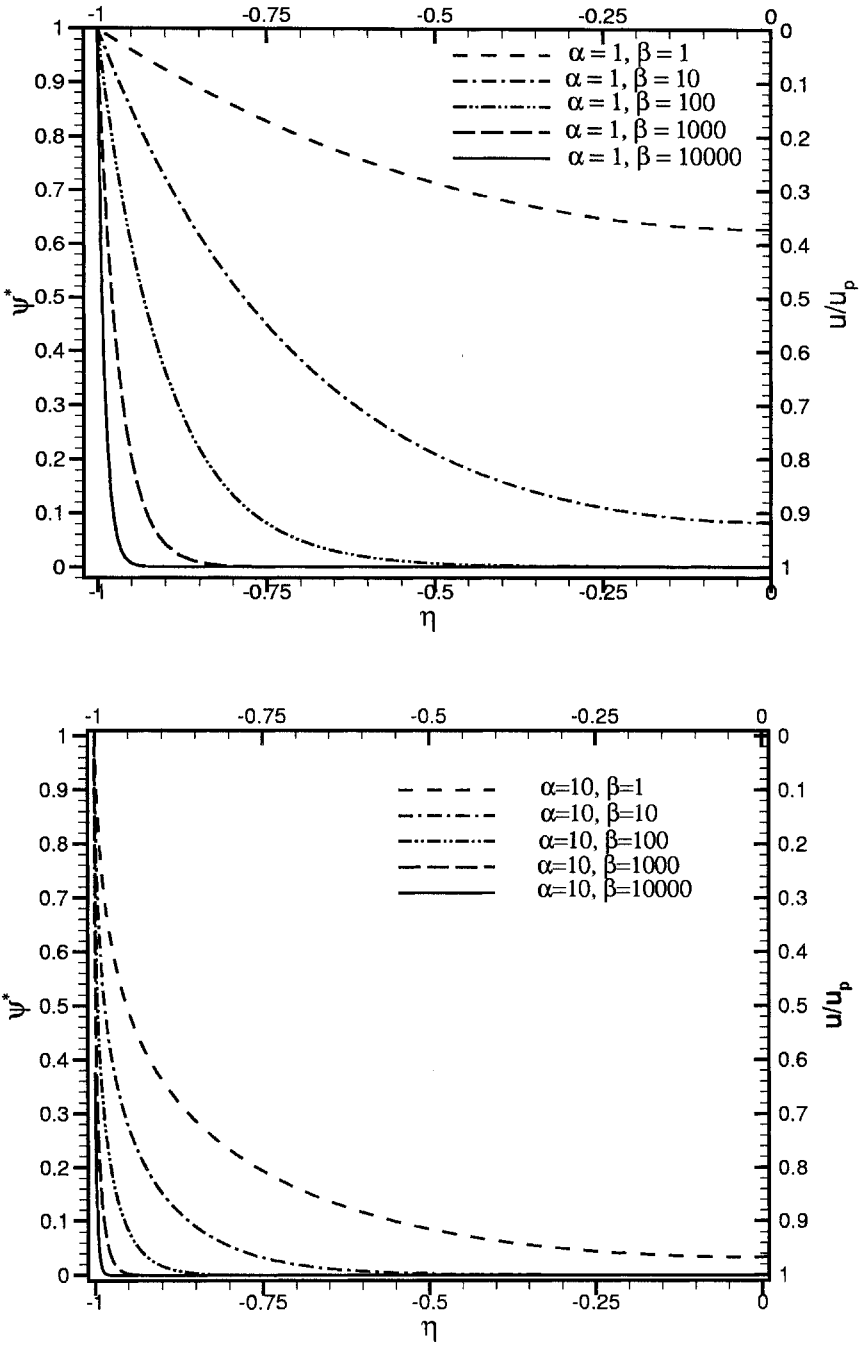

Figure 1. Variation of normalized electroosmotic potential ψ^* and streamwise velocity u/u_p across the half channel for various values of α and β.

4. The solvent is continuous and its permittivity is not affected by the overall and local electric field strength.
5. The ions are point charges.

Numerical Formulation and Validation

We used the h/p type spectral element method to solve of the Poisson–Boltzmann Eq. (3) and incompressible Navier–Stokes equations given by Eq. (8). The numerical algorithm employs *modal spectral expansions* in quadrilateral and unstructured triangular meshes [21]. Hence we can discretize complex engineering geometries with great flexibility due to the unstructured grid and can still maintain the high-order numerical accuracy. The details for numerical discretizations used for the Navier–Stokes equations with arbitrary body forces are given in [22].

The weak variational form of Eq. (3) is solved via a Galerkin projection. A Newton iteration strategy for a variable coefficient Helmholtz equation is utilized to treat exponential nonlinearity in the following form:

$$\left[\nabla^2 - \alpha\beta \cosh(\alpha(\psi^*)^n)\right](\psi^*)^{n+1} = \beta \sinh(\alpha(\psi^*)^n) - \alpha\beta(\psi^*)^n \cosh(\alpha(\psi^*)^n)$$

where n shows the iteration number. The solution of a previous iteration is used for evaluation of the nonlinear forcing function, and the resulting system is solved until the residual is reduced beyond a certain level (typically 10^{-13}). The numerical solution of Eq. (3) is challenging due to the *exponential nonlinearity* associated with the hyperbolic-sine function. Especially for large values of α, the nonlinear forcing increases rapidly for any value of β, making the numerical solution challenging. For very large values of β with $\alpha = 1$, similar difficulties also exist. Accurate resolution of the problem requires high grid density within the EDL. A typical mesh structure is presented in Figure 2*b*. The spectral element mesh has 22 elements across the channel width, spaced in a biased fashion with a minimum width of $0.001\,h$ very near the walls. In the spectral element method the basic mesh structure is fixed, and successively higher values of modal expansions are utilized within each element to further resolve the problem. For rectangular elements shown in Figure 2, $N = 2$ corresponds to a quadratic solution in ψ^*, typically utilized by finite-element algorithms.

We used Eq. (7) directly to determine the numerical accuracy of our results. In Figure 2*a* we present variation of the L_2 error as a function of the modal expansion order N. The results are obtained for the mesh topology shown in Figure 2*b*. Convergence results for $\alpha = 1$, $\beta = 10{,}000$ and $\alpha = 10$, $\beta = 10{,}000$ are presented. The L_2 error norm is defined as

$$L_2 = \frac{\left[\int_\Omega R(\psi^m)^2 d\Omega\right]^{1/2}}{\int_\Omega d\Omega}$$

where Ω shows the entire flow domain. The residual of Eq. (7) is given by

$$R(\psi^m) = \psi^m - \frac{4}{\alpha}\tanh^{-1}\left[\tanh\left(\frac{\alpha}{4}\right)\exp\left(-\sqrt{\alpha\beta}\,\eta^*\right)\right] \tag{11}$$

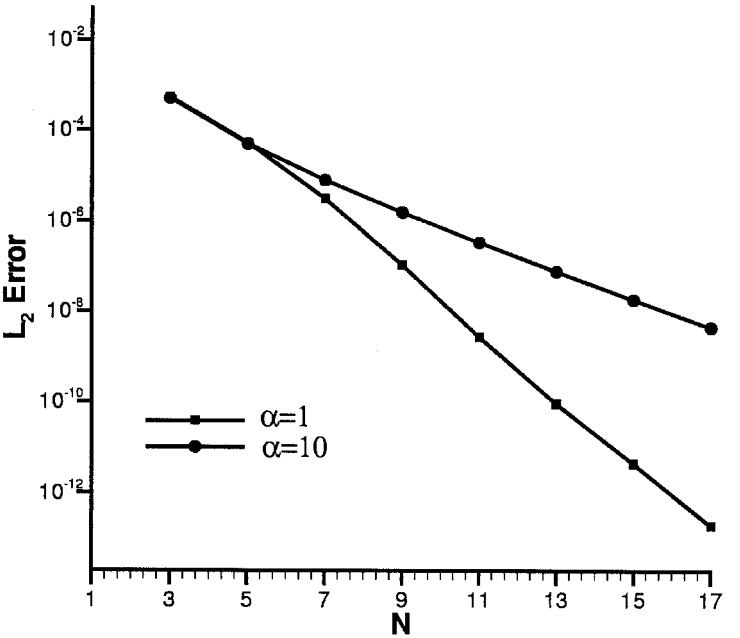

(a)

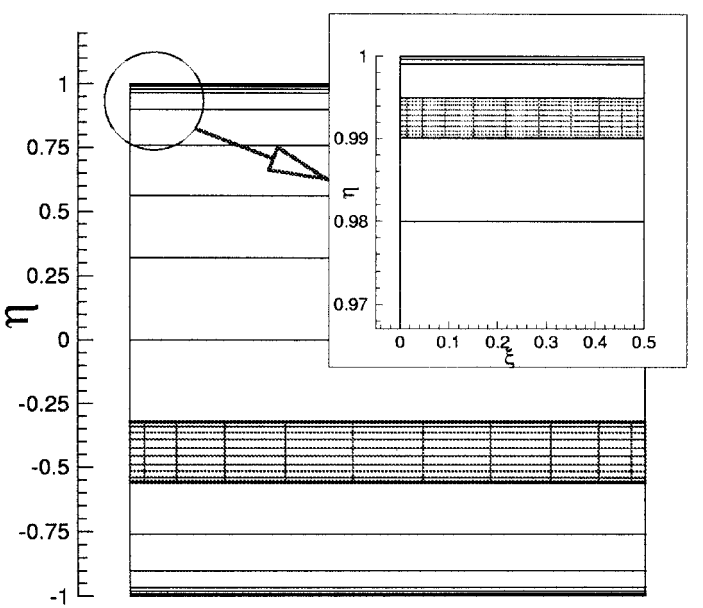

(b)

Figure 2. Spectral convergence in the L_2 error norm as a function of the spectral expansion order N (*a*). Sample grid used to resolve the sharp EDL (*b*) consists of 22 elements across the channel, and each element is discretized with Nth-order modal expansions per direction. The quadrature points for subelemental discretization for select elements are also shown. Simulations are performed for $\beta = 10{,}000$.

where the superscript m shows the numerical results. The convergence results presented in Figure 2 show *exponential decay of the discretization error* with increased N, typical of the spectral element methodology. This high resolution capacity enables us to accurately resolve the EDLs with relatively fewer elements compared with the low-order finite element schemes. Figure 2 shows exponential convergence for both $\alpha = 1$ and $\alpha = 10$ cases. However, the convergence rate for $\alpha = 10$ is significantly slower than the $\alpha = 1$ case, due to the much sharper variations of the electroosmotic potential for increased values of α. A comparison of electroosmotic potential variations for $\alpha = 1$ and $\alpha = 10$ at a fixed value of β can be seen in Figure 1.

NUMERICAL RESULTS FOR STRAIGHT CHANNELS

Let us consider a channel made out of two different materials. The first material exhibits negligible electroosmotic effects, and it is used at the entry and exit portions of the channel. The second material, on the other hand, exhibits strong electroosmotic effects, and it is used in the middle section of the channel. This configuration is shown in Figure 3. It may be possible to fabricate such a microchannel by using different materials (conductors and insulators) on various portions of the channel surface. In practice, it is also possible to obtain variations in the wall potential due to the contamination in the capillary walls, variations in the wall coating, or gradients in the buffer pH [4]. Therefore, the proposed configuration has some practical relevance, and it is a suitable testbed to study mixed electroosmotic/pressure driven flows.

In our simulations, we specified the volumetric flowrate at the channel entrance and calculated the corresponding velocity and pressure distributions in the rest of the channel by numerical solution of Eqs. (3), (8), and (9). In the numerical scheme, we normalized the velocity components with the Helmholtz–Smoluchowski electroosmotic velocity $u_p = -\varepsilon\zeta E_x/\mu$ (i.e., $U = u/u_p$ and $V = v/u_p$), pressure with $\mu u_p/h$, and streamwise coordinate (x) with the half channel height h ($\xi = x/h$). The analytical solution of the mixed electroosmotic/pressure driven channel flow is presented in [23]. The normalized flow velocity in the mixed zone is

$$U(\eta) = -\frac{1}{2}\frac{dP^*}{d\xi}\left(1-\eta^2\right) + 1 - \psi^*(\eta) \tag{12}$$

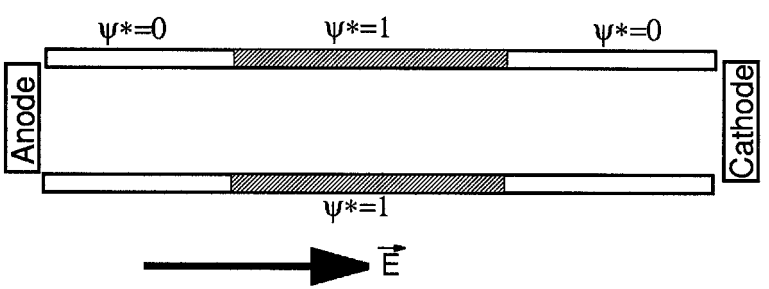

Figure 3. Schematic view of mixed electroosmotic/pressure driven flow channel. The inlet and exit portions of the channel have negligible electroosmotic effects.

For pure electroosmotic flows, $U(\eta) = 1 - \psi^*(\eta)$. This solution is given in Figure 1 for various values of α and β. The normalized pressure gradient in the mixed region is expressed as

$$\frac{dP^*}{d\xi} = 3\left(1 - \frac{\delta^*}{\sqrt{\alpha\beta}}\right) - \frac{3}{2}\dot{Q} \tag{13}$$

where the EDL displacement thickness δ^* is defined as [23]

$$\delta^* = \sqrt{\alpha\beta}\int_0^1 \psi^* d\eta$$

Typical δ^* values are presented in Table 1 as a function of α. Therefore, one can use δ^* to obtain relationships for the velocity and pressure distributions for mixed electroosmotic/pressure driven channel flows. The analytical expression for the normalized wall shear stress is

$$\tau_w^* = \sqrt{\frac{\beta}{\alpha}}\sqrt{2\cosh(\alpha) - 2\cosh(\alpha\psi_c)} - \frac{dP^*}{d\xi} \tag{14}$$

In this article, we compare our numerical results with the above analytical expressions. To eliminate the channel entry effects, we specified a parabolic velocity profile at the inlet with a maximum inlet velocity of $U_{in} = u_{in}/u_p$. Using U_{in} we can generate various levels of pressure gradients in the mixed electroosmotic/pressure driven zone. The numerical simulations are performed for Re = 0.005, where Re is based on the average channel velocity and the half channel height. We kept the streamwise electric field strength and the EDL properties constant at $\alpha = 1$ (corresponding to $\zeta = -25.4\,\text{mV}$) and $\beta = 10{,}000$. Therefore, the Debye length in the simulations is about 1/100th of the channel half height, and we resolve the entire flow domain, including the EDL.

In Figure 4 we present nondimensional pressure distribution along the channels for various values of U_{in}. The numerical algorithm specifies zero gauge pressure at the channel outlet. Hence, all numerical results show zero gauge pressure at the exit. The entry and the exit portions of the channels are pure pressure driven, and the electroosmotic forces are present only at $3.1 \leq \xi \leq 6.2$. The effective electric field is in the positive streamwise direction. Figure 4 shows variation of channel centerline pressure as a function of various U_{in} values. Using Eq. (13) we can estimate the theoretical value of U_{in} that results in a desired pressure gradient in the mixed region. For example, the theoretical value of $U_{in} = 1.485$ for $\alpha = 1$ and $\beta = 10{,}000$ gives zero pressure gradient in the mixed electroosmotic pressure driven flow region. The analytical and numerical predictions of the pressure gradients at this mixed region

Table 1. Variation of the EDL displacement thickness δ^* as a function of the ionic energy parameter α. (Data from [23].)

α	1	3	5	7	10	15
δ^*	0.98635	0.89156	0.75670	0.62702	0.47731	0.32765

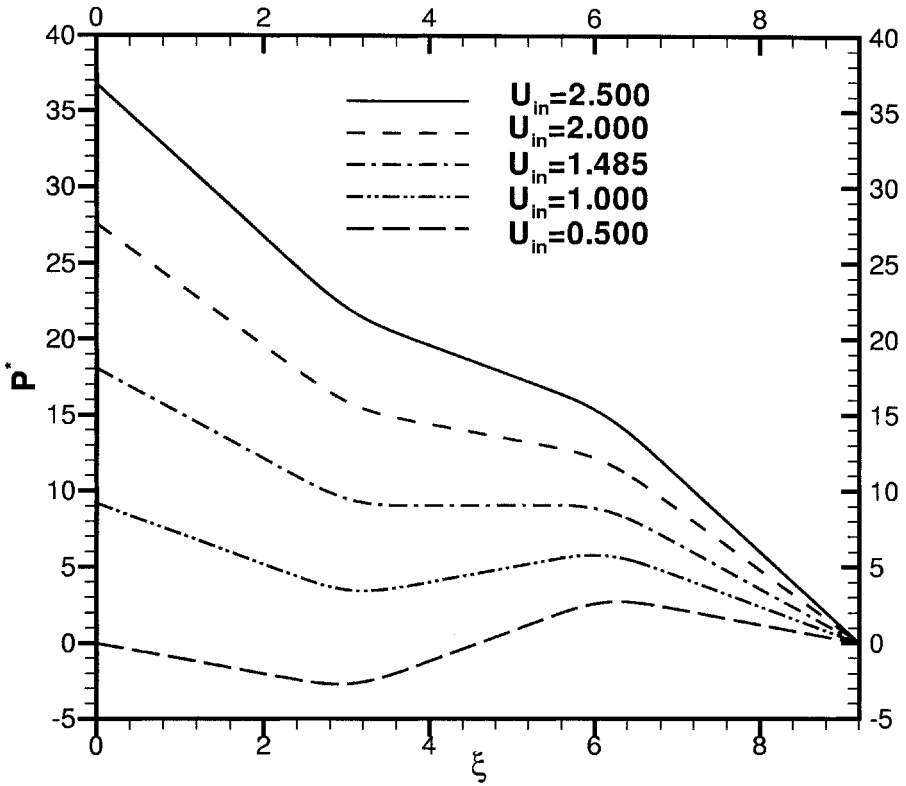

Figure 4. The normalized pressure distribution in a mixed electroosmotic/pressure driven channel for various values of U_{in}. The case $U_{in} = 1.485$ corresponds to the "plug-like flow." The electroosmotic forces are present only at $3.1 \leq \xi \leq 6.2$. Simulation results are for $\alpha = 1$, $\beta = 10{,}000$, and $Re = 0.005$.

are presented in Table 2 for various values of U_{in}. The theoretical and numerical predictions agree within 0.3%, consistent with the convergence results shown in Figure 2.

The corresponding velocity profiles across the channel at $\xi = 4.5$ are presented in Figure 5. A "plug-like velocity" profile is observed for $U_{in} = 1.485$, as predicted by the theory. The velocity profiles for favorable and adverse pressure gradient flows

Table 2. The numerical and analytical estimates of the pressure gradient Eq. (13) and wall shear stress Eq. (14) in the mixed electroosmotic pressure driven flow regime. Differences between the numerical results and the analytical formulas are less than 0.3% for a seventh-order spectral element discretization for the $\alpha = 1$, $\beta = 10{,}000$ case. The numerical error is consistent with the convergence results shown in Figure 2.

$U_{in} = \frac{u_{in}}{u_P}$	$dP^*_{num}/d\xi$	$dP^*_{ana}/d\xi$	$\tau_{w(num)}$	$\tau_{w(ana)}$
2.500	− 2.0268	− 2.0296	106.334	106.249
2.000	− 1.0284	− 1.0296	105.334	105.249
1.485	0.0000	0.0000	104.301	104.219
1.000	0.9734	0.9704	103.334	103.249
0.500	1.9676	1.9704	102.334	102.249

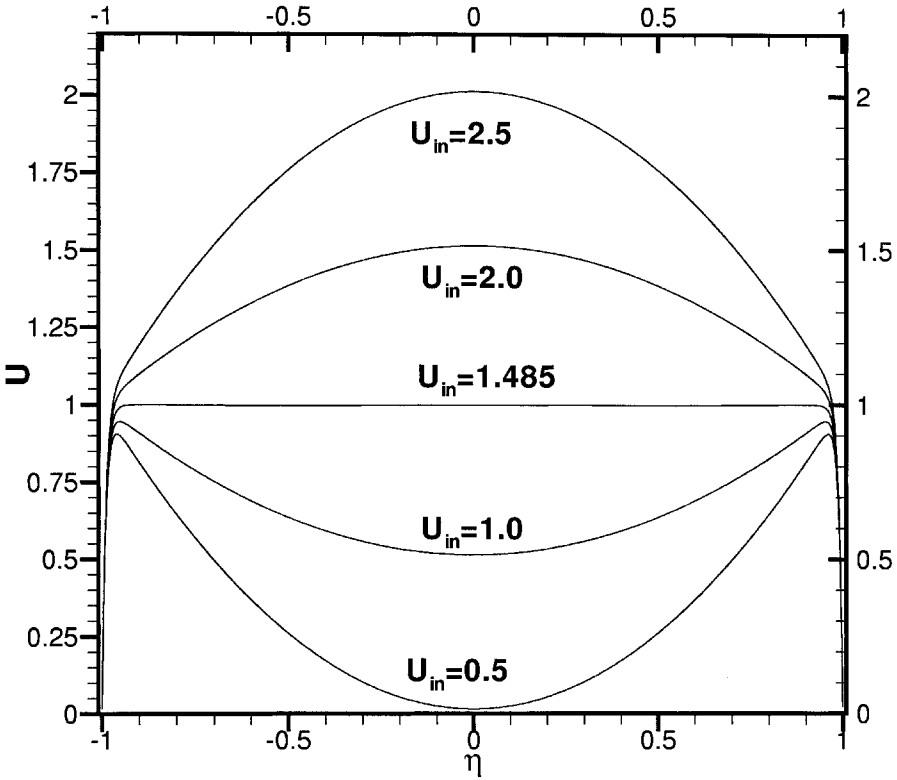

Figure 5. The velocity distribution in a mixed electroosmotic/pressure driven channel for various values of U_{in}. The case $U_{in} = 1.485$ corresponds to the "plug-like flow." For larger and smaller values of U_{in}, we obtain favorable and adverse pressure gradients, respectively. Simulation results are for $\alpha = 1$, $\beta = 10,000$, and $\mathrm{Re} = 0.005$.

are also presented in Figure 5. For example, $U_{in} = 2.5$ corresponds to a favorable pressure gradient case, which is a combination of a plug-like flow with a parabola in the bulk of the channel. The corresponding pressure variation shown in Figure 4 indicates significant pressure drops at the entry and the exit portions of the channel. However, in the mixed zone, the pressure drop is relatively low due to the electroosmotic pumping.

The adverse pressure gradient case of $U_{in} = 0.5$ is an *electrokinetically driven micropump*. For this case, the inlet and the exit pressures are the same, corresponding to the *laboratory on a chip* device that is exposed to atmospheric pressure at both ends. The entire flow is driven by the electrokinetic forces, which overcome the drag force within the entire channel system. The pressure drops at the inlet and exit portions of the channel ($\xi \leq 3.1$ and $\xi \geq 6.2$) are due to the shear stress. A micropump must be able to raise the system pressure to be able to drive the flow. The electroosmotic pump is doing precisely this. The net pressure gradient is positive within the pump, as shown in Figure 4. Here we must note that in a pure electroosmotic system, the plug-like velocity profiles with zero-pressure gradient will be obtained. In the case of $U_{in} = 0.5$, an adverse pressure gradient is present to overcome the pressure drop at the inlet and

exit sections. Hence, any mixed flow system should exhibit a behavior similar to our simulation results presented in Figure 4. The velocity profile for this case indicates a combination of plug and adverse pressure gradient channel flow behavior, and the net volumetric flowrate is positive, as shown in Figure 5.

The shear stress in the mixed electroosmotic pressure driven flow region is enhanced due to the presence of the EDL and the pressure gradients. Comparisons of shear stress estimates obtained by numerical simulations and the analytical Eq. (14) are also presented in Table 2. The error in the numerical results are less than 0.1%.

For a closed system it is possible to create large pressure gradients using electroosmotic forces. These can be used for microscale actuation of micropistons or microbellow mechanisms. We simulated such a configuration by closing the exit of our channel. Due to the presence of the electroosmotic forces, the pressure raises linearly within the electroosmotic region, as shown in Figure 6. This pressure rise is accompanied by the electroosmotic flow near channel walls and a reverse flow in the middle of the microchannel, as shown in Figure 6.

FLOW CONTROL IN A T-JUNCTION

The electroosmotic effects can be selectively introduced for flow control in complex microgeometries. In Figure 7 we present the T-junction geometry, which is widely used for species separation, DNA sequencing, electrokinetic focusing, and immunoassays. A dielectric material of $\zeta = -25.4$ mV is used for channel BC. On the other hand an electroosmosis surpressing material is used for the side arm A. The corresponding boundary conditions for the T-junction are shown in Figure 7*b*. We assumed that the buffer solution is water and the ion concentration density is $n_o = 10^{-5}$ M. The simulation results presented here are performed for a channel half height of $h = 10\,\mu$m, corresponding to $\alpha = 1$, $\beta = 10{,}000$. The Reynolds number based on the average channel velocity is $\mathrm{Re} = 0.005$, which is practically Stokes flow with local electroosmotic body forces.

For flow manipulation purposes, an external electric field is applied using an anode/cathode pair far upstream and downstream of the branches A and C, respectively. Due to the geometric complexity, the electric field is strongly two dimensional immediately near the junction. However, it reaches a *constant unidirectional value* in branches A and C, far away from the T-junction. This constant electric field value is used as the reference electric field E_{AC} to characterize the flow response. To normalize E_{AC}, we defined E_o, which corresponds to a plug flow electric field in a straight channel with *identical length and electrochemical conditions*. For the aforementioned dimensional values, $\|\vec{E}_o\| = 282$ V/cm. Normalization of the external electric field is desired to obtain nondimensional characteristics of the microfluidic system. Hence, flow control results are presented as a function of the E_{AC}/E_o ratio.

The numerical simulations are performed by specifying the flowrate at the domain entrance A, using a fully developed parabolic velocity profile. Since there are no EDL effects in channel A, the flow remains parabolic until it reaches the junction. The electroosmotic effects are present at the junction primarily in branch C. By systematically varying the external electric field strength E_{AC}, we studied the

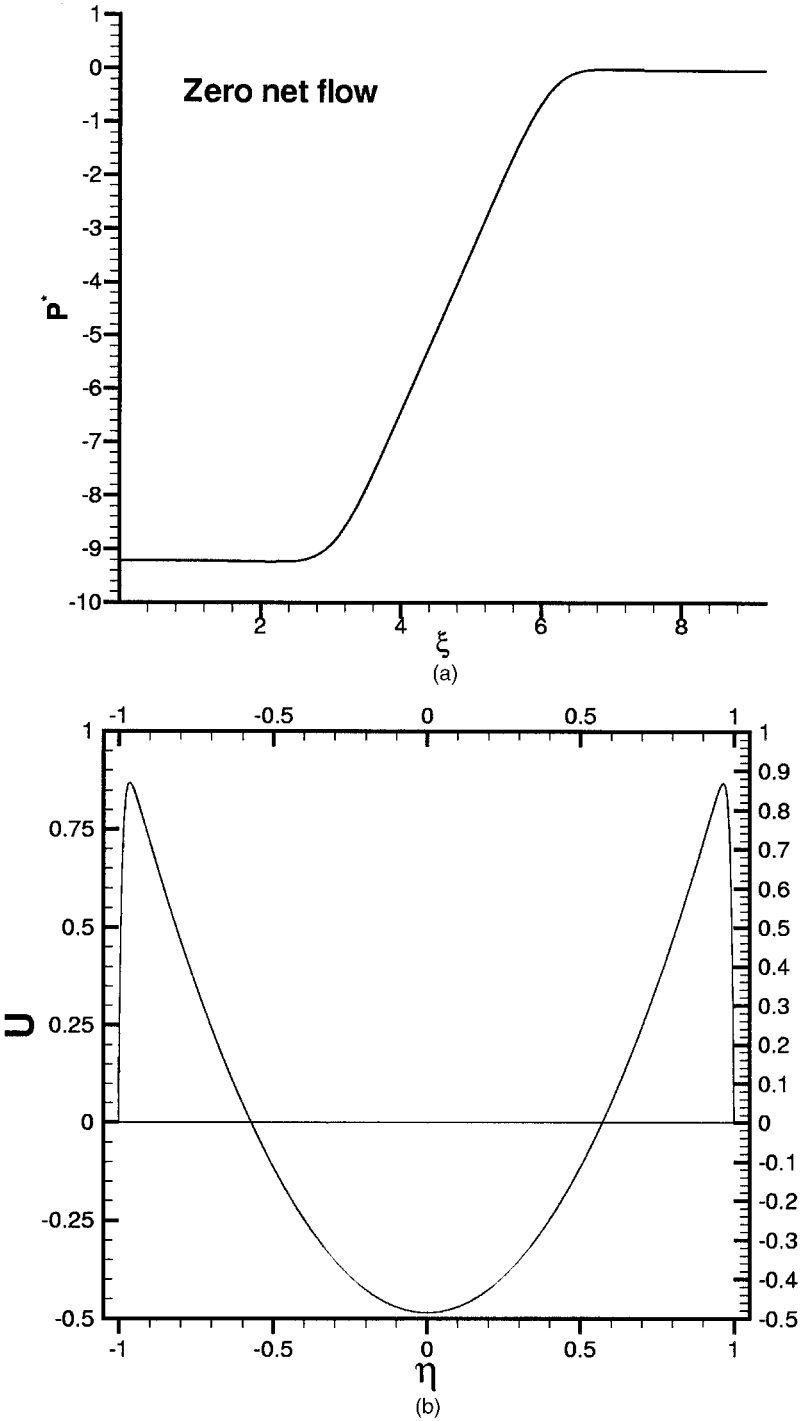

Figure 6. Pressure buildup along the microchannel for zero net flow (*a*); and the corresponding velocity distribution across the channel (*b*).

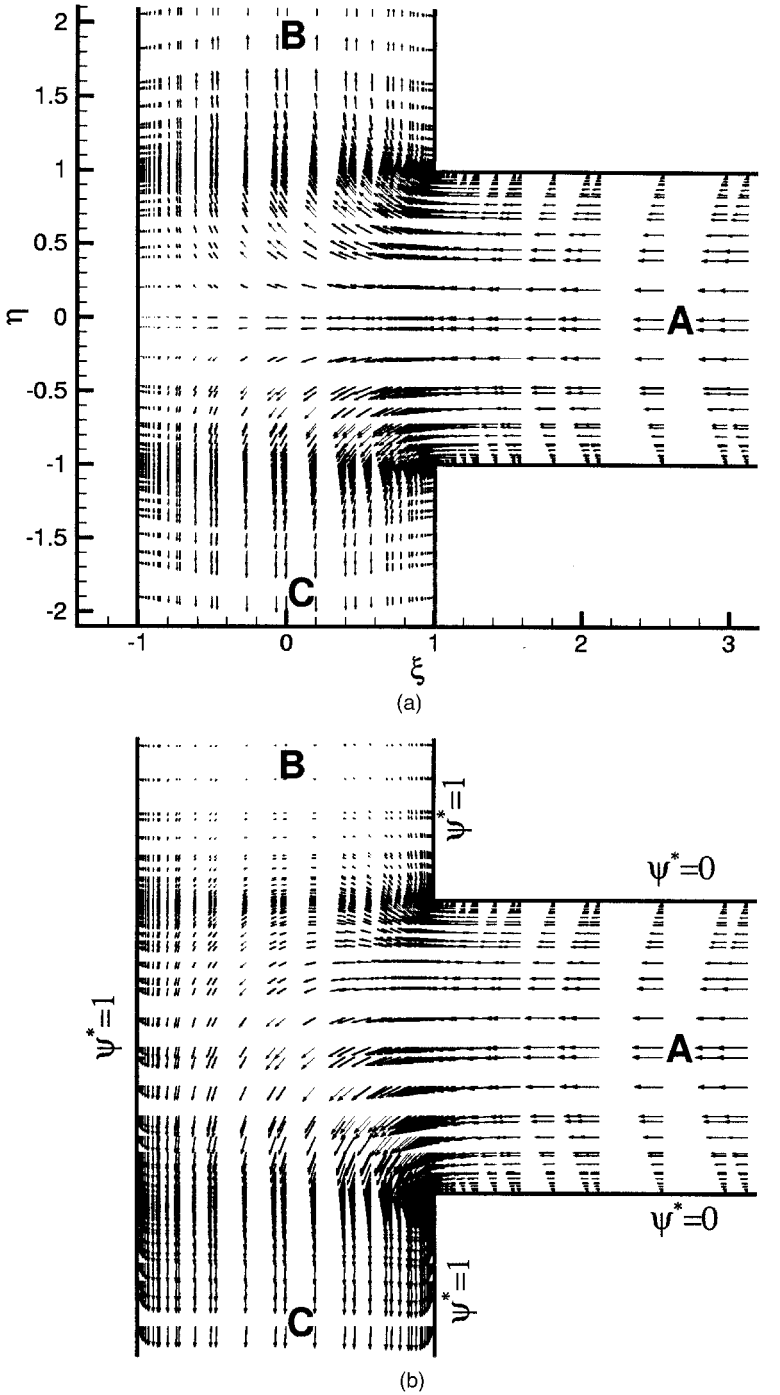

Figure 7. Velocity vectors for electroosmotic flow in a T-junction. The simulations are performed for $\alpha = 1$ and $\beta = 10{,}000$ at $\mathrm{Re} = 0.005$. (*a*) Zero external electric field; (*b*) external electric field $E_{AC} = 1.043E_o$. The electroosmotic potential boundary conditions are shown also.

combined effects of pressure and viscous and electroosmotic body forces in section *C*, and demonstrated flow control in the branches of the T-junction.

Figure 7*a* shows velocity vectors for the T-junction with zero electric field. Under this condition, the pressure driven flow is divided uniformly into branches *B* and *C*. The figure shows an enlarged view of the computational domain. The inlet and outlet boundary conditions are imposed sufficiently away from the T-junction. Only 25% of the velocity vectors are shown in order not to clutter the figure. The spectral element mesh and the spectral expansion order ($N = 7$) are consistent with the convergence results shown in Figure 2. A numerical resolution study conducted by p-type refinements (i.e., increasing the spectral expansion order) did not affect the solution, indicating grid independence of the results.

Flow control is obtained by applying an electric field E_{AC}. One representative case is $E_{AC} = 1.043E_o$, where the *entire flow* is deflected toward branch *C*. The velocity vectors for this case are shown in Figure 7*b*. Figure 8 shows the flowrate in the *B* and *C* branches as a function of the E_{AC}/E_o. The flowrate in each branch can be altered by changing E_{AC}. For $E_{AC} = 1.043E_o$, the flow in branch B is *completely blocked*. Since, E_o correspond to a plug flow in a straight channel under identical length and electrochemical conditions, the 4.3% increase in the electric field for this

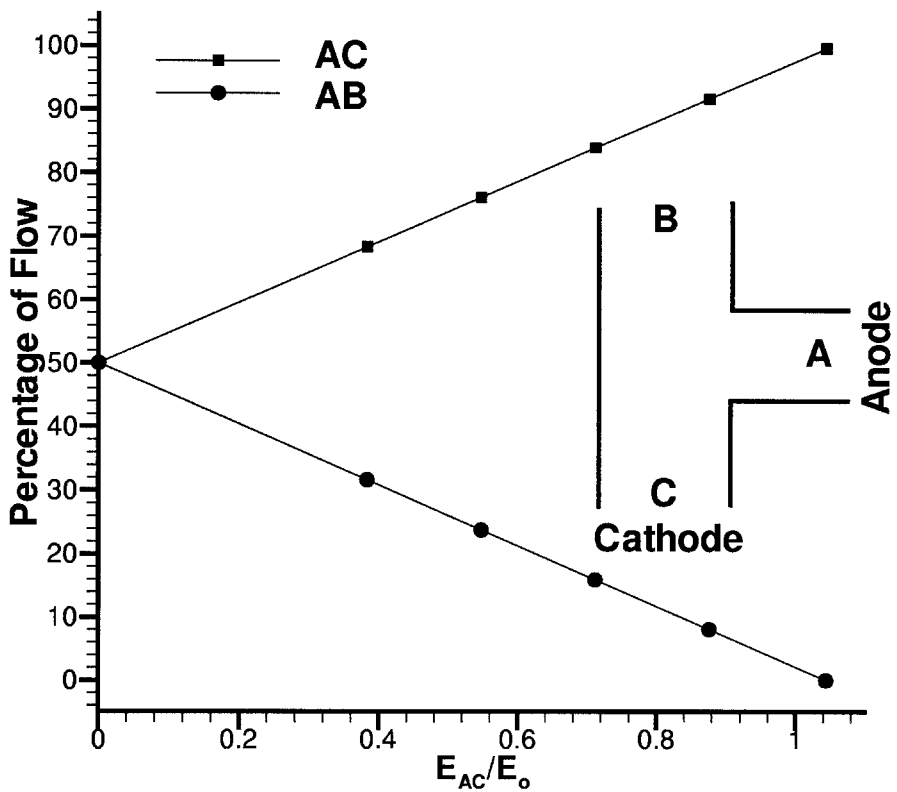

Figure 8. Flow rate variation in the branches of the T-junction as a function of the externally applied electric field E_{AC}/E_o.

case is due to the *two dimensionality and corner effects* in the T-junction. If E_{AC} is increased beyond $1.043E_o$, the flowrate in branch C will be further increased, resulting in suction from branch B. We did not try this case, in order to *avoid suction from the outflow boundary B*, where zero Neumann conditions on the velocity components are imposed.

DISCUSSION

We presented numerical simulation results for mixed electroosmotic/pressure driven flows in straight channels and T-junction geometry. The simulations are performed for specified inlet flowrate conditions, and the electroosmotic forces are applied *locally* for flow control. In straight channels, we demonstrated electrokinetic pumping and mechanisms for creating large pressure variations in closed systems. In the T-junction, we have shown that the *flowrate variation as a function of the electric field is linear* in the Stokes flow regime. Hence, the T-junction channel can be used as an electroosmotically actuated microvalve with nonmoving components. The *linear response* of the device allows *precise flowrate control* for various micro-fluidic applications.

We developed a spectral element algorithm for solution of the Poisson–Boltzmann and the Navier–Stokes equations, and we have formally shown exponential convergence of our algorithm. Due to the difficulties associated with experimenting in microscales, it is desirable to develop reliable numerical models that can *accurately describe* microfludic transport in *complex microgeometries*. Our numerical methodology has the flexibility of utilizing mixed unstructured/structured grid topology for discretization of complex geometries, and at the same time it delivers *high-order accuracy*. Hence, this numerical algorithm can be used for designing *optimized* microfluidic systems *prior* to hardware fabrication and experimental verification.

REFERENCES

1. D. Burgreen and F. R. Nakache, Eletrokinetic Flow in Ultrafine Capillary Silts, *J. Phys. Chem.*, vol. 68, no. 5, pp. 1084–1091, 1964.
2. C. L. Rice and R. Whitehead, Electro Kinetic Flow in a Narrow Cylindrical Capillary, *J. Phys. Chem.*, vol. 69, pp. 4017–4023, 1965.
3. H. J. Keh and Y. C. Liu, Electroosmotic Flow in a Circular Capillary with a Surface Charge Layer, *J. Colloid and Interface Surfaces*, vol. 172, pp. 222–229, 1995.
4. J. M. Molho, A. E. Herr, M. Desphande, J. R. Gilbert, M. G. Garguilo, P. H. Paul, P. M. John, T. M. Woudenberg, and C. Connel, Fluid Tranport Mechanisms in Micro Fluidic Devices, in *Proc. 1998 ASME Micro-Electro-Mechanical-Systems (MEMS)*, Los Angeles, CA, pp. 69–75, 1998.
5. P. H. Paul, M. G. Graguilo, and D. J. Rakestraw, Imaging of Pressure and Electrokinetically Driven Flows Through Open Capillaries, *Analytical Chemistry*, vol. 70, pp. 2459–2467, 1998.
6. E. B. Cummings, S. K. Griffiths, and R. H. Nilson, Irrotationality of Uniform Electroosmosis, in *Proc. SPIE Microfluidic devices and systems* II, Santa Clara, CA, 1999.
7. E. B. Cummings, S. K. Griffiths, R. H. Nilson, and P. H. Paul, Conditions for Similitude Between the Fluid Velocity and Electric Field in Electroosmotic Flow, *Analytical Chemistry*, vol. 72, pp. 2526–2532, 2000.

8. A. E. Herr, J. I. Molho, J. G. Santiago, M. G. Mungal, T. W. Kenny, and M. G. Garguilo, Electroosmotic Capillary Flow with Non Uniform Zeta Potential, *Analytical Chemistry*, vol. 72, pp. 1053–1057, 2000.
9. S. C. Jacobson, T. E. McKnight, and J. M. Ramsey, Microfluidic Devices for Electrokinetically Driven Parallel and Serial Mixing, *Analytical Chemistry*, vol. 71, pp. 4455–4459, 1999.
10. N. A. Polson and M. A. Hayes, Electroosmotic Flow Control of Fluids on a Capillary Electrophoresis Microdevice Using an Applied External Voltage, *Analytical Chemistry*, vol. 72, no. 10, pp. 1088–1092, 2000.
11. C. Yang and D. Li, Analysis of Electrokinetic Effects on the Liquid Flow in Rectangular Microchannels, *J. Colloids and Surfaces*, vol. 143, pp. 339–353, 1998.
12. C. Yang, D. Li, and J. H. Masliyah, Modeling Forced Liquid Convection in Rectangular Microchannels with Electrokinetic Effects, *Int. J. Heat Mass Trans.*, vol. 41, pp. 4229–4249, 1998.
13. J. Pfahler, J. Harley, H. Bau, and J. Zemel, Gas and Liquid Flow in Small Channels, in *Proc. ASME Winter Annual Meeting*, DSC, pp. 49–59, 1991.
14. N. A. Patankar and H. H. Hu, Numerical Simulation of Electroosmotic Flow, *Analytical Chemistry*, vol. 70, pp. 1870–1881, 1998.
15. S. V. Ermakov, S. C. Jacobson, and J. M. Ramsey, Computer Simulation of Electrokinetic Transport in Micro Fabricated Channel Structures, *Analytical Chemistry*, vol. 70, pp. 4494–4504, 1998.
16. F. Bianchi, R. Ferrigno, and H. H. Girault, Finite Element Simulation of an Electroosmotic-Driven Flow Division at a T-junction of Microscale Dimension, *Analytical Chemistry*, vol. 72, pp. 1987–1993, 2000.
17. G. M. Mala, D. Li, and J. D. Dale, Heat Transfer and Fluid Flow in Microchannels, *Int J. Heat Mass Trans.*, vol. 40, pp. 3079–3088, 1997.
18. R. F. Probstein, *Physiochemical Hydrodynamics*, 2nd ed., Wiley and Sons Inc., New York, 1994.
19. A. W. Adamson, *Physical Chemistry of Surfaces*, Wiley Interscience Publication, New York, 1990.
20. R. J. Hunter, *Zeta Potential in Colloid Science: Principles and Applications*, Academic Press Inc., New York, 1981.
21. G. E. Karniadakis and S. J. Sherwin, *Spectral/HP Element Methods for CFD*, Oxford University Press, Oxford, UK, 1999.
22. T. C. Warburton. *Spectral/hp Methods on Polymorphic Multi-Domains: Algorithms and Applications*, Ph.D. dissertation, Brown University, Providence, RI, 1999.
23. P. Dutta and A. Beskok, Analytical Solution of Combined Electroosmotic/Pressure Driven Flows in Two-Dimensional Straight Channel, *Analytical Chemistry*, vol. 73, pp. 1979–1986, 2001